

Electronic Supplementary Information (ESI) for:

**Shedding light on ultrafast ring-twisting pathways of halogenated  
GFP chromophores from the excited to ground state**

Sean A. Boulanger<sup>1</sup>, Cheng Chen<sup>1</sup>, Longteng Tang<sup>1</sup>, Liangdong Zhu<sup>1</sup>, Nadezhda S. Baleeva<sup>2,3</sup>,

Ivan N. Myasnyanko<sup>2,3</sup>, Mikhail S. Baranov<sup>2,3</sup>, and Chong Fang<sup>\*,1</sup>

<sup>1</sup>Department of Chemistry, Oregon State University, 153 Gilbert Hall, Corvallis, Oregon 97331,  
United States

<sup>2</sup>Institute of Bioorganic Chemistry, Russian Academy of Sciences, Miklukho-Maklaya 16/10,  
Moscow 117997, Russia

<sup>3</sup>Pirogov Russian National Research Medical University, Ostrovitianov 1, Moscow 117997,  
Russia

\*To whom correspondence should be address. E-mail: [Chong.Fang@oregonstate.edu](mailto:Chong.Fang@oregonstate.edu).

## **Table of Contents**

Page number

### **ESI Text**

**S4–6**

General procedure for the synthesis of (*Z*)-5-arylidene-2,3-dimethyl-3,5-dihydro-4*H*-imidazol-4-ones S4

Synthesis of the mono- and dihalogenated HBDI derivatives S4–6

### **ESI Figures**

**S7–16**

**Figure S1.**  $pK_a$  titration curves for *p*-HBDI and monohalogenated HBDI derivatives S7

**Figure S2.**  $pK_a$  titration curves for dihalogenated HBDI derivatives S8

**Figure S3.** Fluorescence quantum yield (FQY) measurements of HBDI derivatives S9–10

**Figure S4.** Determination of molar extinction coefficients for HBDI derivatives S11

**Figure S5.** Fluorescence quantum yield plotted against HOMO-LUMO energy gap S12

**Figure S6.** Ground-state energies by scanning two dihedral angles along the P- and I-ring isomerization coordinates from quantum calculations S13–14

**Figure S7.** Global analysis of the fs-TA spectra of HBDI derivatives S15

**Figure S8.** Frequency shift of a Raman marker band ( $\sim 1560\text{ cm}^{-1}$ ) in ground- and early/late excited-state FSRS S16

### **ESI Tables**

**S17–25**

**Table S1.** Selected data from steady-state electronic spectroscopy and parameters obtained from the simplified Strickler-Berg equation for various HBDI derivatives S17

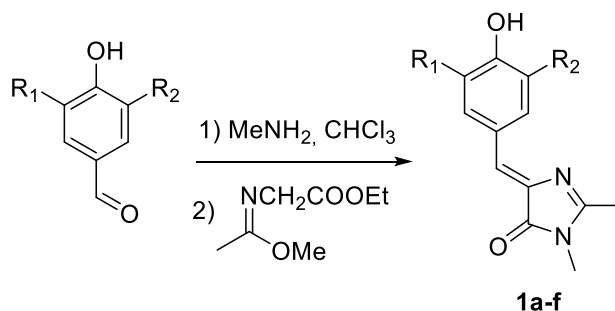
**Table S2.** Ground-state Raman mode assignments of monohalogenated HBDI S18–19

**Table S3.** Ground-state Raman mode assignments of dihalogenated HBDI S20–21

**Table S4.** Excited-state Raman mode assignments of monohalogenated HBDI S22

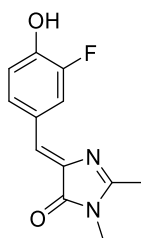
<b>Table S5.</b> Excited-state Raman mode assignments of dihalogenated HBDI	S23
<b>Table S6.</b> NBO charges for separate moieties of various HBDI derivatives	S24–25
<b>ESI References</b> (with full authorship of the Gaussian 09 software)	<b>S26–28</b>
<b>ESI Appendix</b>	<b>S29–30</b>
<b>Appendix S1.</b> $^1\text{H}$ NMR spectrum of the new Cl-HBDI compound	S29
<b>Appendix S2.</b> $^{13}\text{C}$ NMR spectra of the new Cl-HBDI compound	S30

## ESI Text



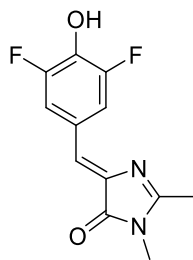
**General procedure for the synthesis of (Z)-5-arylidene-2,3-dimethyl-3,5-dihydro-4H-imidazol-4-ones (1a-f, see below for details).** To the solution of corresponding aldehyde (20 mmol) in chloroform (100 mL), a 40% aqueous methylamine solution (60 mmol) and anhydrous sodium sulfate (20 g) were added. The mixture was stirred for 48 h at room temperature, then filtered and dried over the additional Na<sub>2</sub>SO<sub>4</sub>. After solvent evaporation, ethyl ((1-methoxy)amino)acetate<sup>1</sup> (3.5 g, 22 mmol) and methanol (3 mL) were added. The mixture solution was stirred for 24 h at room temperature, after solvent removal in vacuum, the resultant product **1** was purified by column chromatography (CHCl<sub>3</sub>–EtOH at 20:1).<sup>2</sup>

### **Synthesis procedures of the mono- and dihalogenated HBDI derivatives.**



#### **(Z)-5-(3-fluoro-4-hydroxybenzylidene)-2,3-dimethyl-3,5-dihydro-4H-imidazol-4-one (1a)**

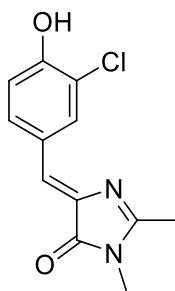
(R<sub>1</sub>=H, R<sub>2</sub>=F) Yellow solid (1.82 g, 39%); <sup>1</sup>H NMR (700 MHz, 303 K, DMSO-d<sub>6</sub>) δ ppm 10.52 (br. s., 1H), 8.19 (dd, *J* = 13.1, 1.8 Hz, 1H), 7.76 (dd, *J* = 8.4, 1.7 Hz, 1H), 6.99 (t, *J* = 8.8 Hz, 1H), 6.89 (s, 1H), 3.09 (s, 3H), 2.34 (s, 3H).<sup>3</sup>



**(Z)-5-(3,5-difluoro-4-hydroxybenzylidene)-2,3-dimethyl-3,5-dihydro-4H-imidazol-4-one**

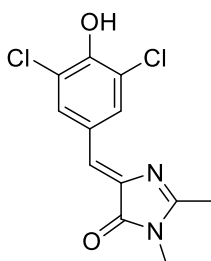
**(1b)** ( $R_1=R_2=F$ )

Yellow solid (3.33 g, 66%);  $^1\text{H NMR}$  (700 MHz, 303 K,  $\text{DMSO-}d_6$ )  $\delta$  ppm 10.88 (s, 1H), 7.96 (d,  $J = 9.7$  Hz, 2H), 6.89 (s, 1H), 3.09 (s, 3H), 2.36 (s, 3H).<sup>3</sup>



**(Z)-5-(3-chloro-4-hydroxybenzylidene)-2,3-dimethyl-3,5-dihydro-4H-imidazol-4-one (1c)**

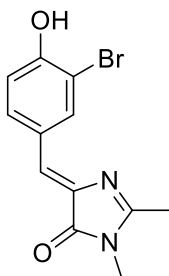
( $R_1=H$ ,  $R_2=Cl$ ) Yellow solid (1.80 g, 36%); m.p. = 268–270 °C;  $^1\text{H NMR}$  (700 MHz, 303 K,  $\text{DMSO-}d_6$ )  $\delta$  ppm 10.82 (s, 1H), 8.36 (d,  $J = 1.8$  Hz, 1H), 7.94 (dd,  $J = 8.4$ , 1.8 Hz, 1H), 7.02 (d,  $J = 8.4$  Hz, 1H), 6.88 (s, 1H), 3.09 (s, 3H), 2.35 (s, 3H) (see Appendix S1);  $^{13}\text{C NMR}$  (176 MHz, 303 K,  $\text{DMSO-}d_6$ )  $\delta$  ppm 169.6, 163.3, 154.8, 137.3, 133.1, 132.4, 126.5, 123.7, 120.1, 116.6, 26.2, 15.3 (see Appendix S2). High-resolution mass spectrum (HRMS) using electrospray ionization (ESI)  $m/z$ : 251.0579 found (calculated for  $\text{C}_{12}\text{H}_{12}\text{ClN}_2\text{O}_2^+$ ,  $[\text{M}+\text{H}]^+$  251.0582).



**(Z)-5-(3,5-dichloro-4-hydroxybenzylidene)-2,3-dimethyl-3,5-dihydro-4H-imidazol-4-one**

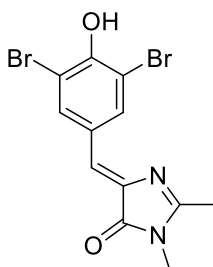
**(1d)** (R<sub>1</sub>=R<sub>2</sub>=Cl)

Yellow solid (2.74 g, 48%); <sup>1</sup>H NMR (700 MHz, 303 K, DMSO-*d*<sub>6</sub>) δ ppm 10.78 (br. s., 1H), 8.28 (s, 2H), 6.89 (s, 1H), 3.09 (s, 3H), 2.36 (s, 3H).<sup>4</sup>



**(Z)-5-(3-bromo-4-hydroxybenzylidene)-2,3-dimethyl-3,5-dihydro-4H-imidazol-4-one (1e)**

(R<sub>1</sub>=H, R<sub>2</sub>=Br) Yellow solid (3.42 g, 58%); <sup>1</sup>H NMR (700 MHz, 303 K, DMSO-*d*<sub>6</sub>) δ ppm 10.89 (s, 1H), 8.50 (d, *J* = 1.9 Hz, 1H), 7.98 (dd, *J* = 8.6, 1.9 Hz, 1H), 7.00 (d, *J* = 8.6 Hz, 1H), 6.87 (s, 1H), 3.09 (s, 3H), 2.35 (s, 3H).<sup>5</sup>



**(Z)-5-(3,5-dibromo-4-hydroxybenzylidene)-2,3-dimethyl-3,5-dihydro-4H-imidazol-4-one**

**(1f)** (R<sub>1</sub>=R<sub>2</sub>=Br)

Yellow solid (2.02 g, 27%); <sup>1</sup>H NMR (700 MHz, 303 K, DMSO-*d*<sub>6</sub>) δ ppm 10.52 (br. s., 1H), 8.46 (s, 2H), 6.89 (s, 1H), 3.09 (s, 3H), 2.36 (s, 3H).<sup>2,4</sup>

## ESI Figures

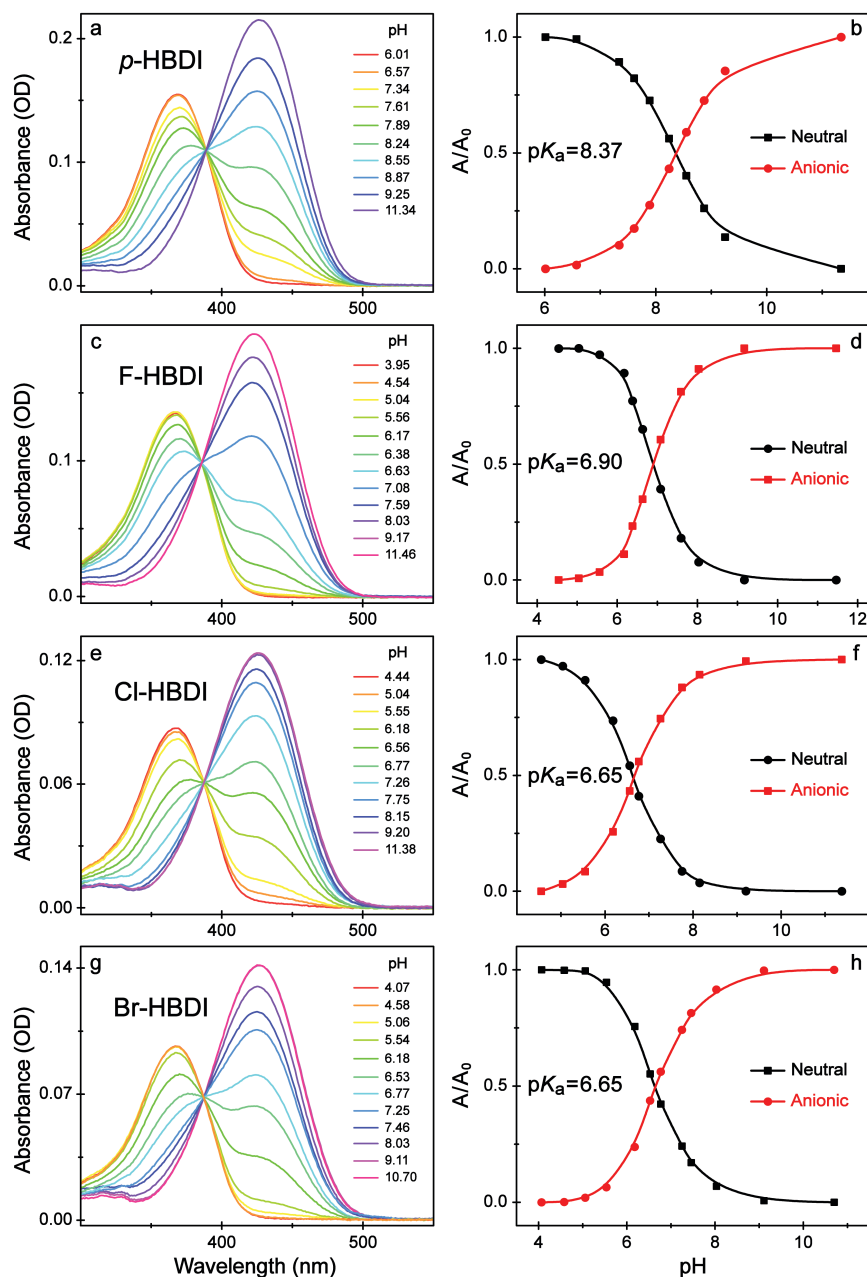


**Figure S1.** Electronic absorption titration curves for the parent and monohalogenated HBDI derivatives. The neutral-to-anionic form absorption spectra of (a) *p*-HBDI and (c, e, and g) monohalogenated HBDI derivatives in aqueous solution with increasing pH values (listed by the color-coded spectra) at room temperature. The pK<sub>a</sub> values are determined from the equivalence points in panels b, d, f, and h for *p*-HBDI, F-HBDI, Cl-HBDI, and Br-HBDI, respectively.<sup>2,3</sup>

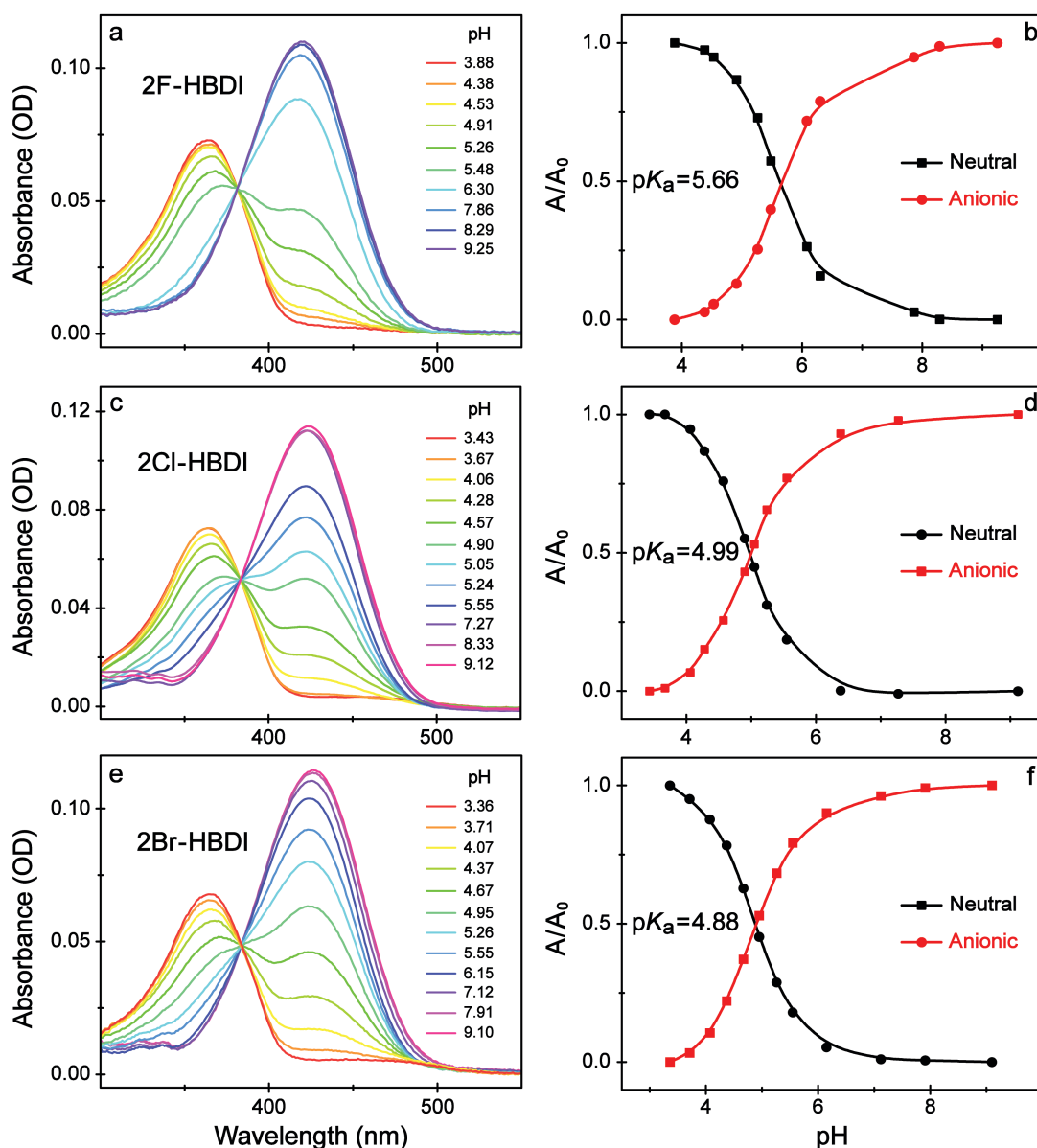


**Figure S2.** Electronic absorption titration curves for dihalogenated HBDI derivatives. The neutral-to-anionic form absorption spectra of (a, c, and e) dihalogenated HBDI derivatives in aqueous solution with increasing pH values (listed by the color-coded spectra) at room temperature. The pK<sub>a</sub> values are determined from the equivalence points in panels b, d, and f for 2F-HBDI, 2Cl-HBDI, and 2Br-HBDI, respectively, and listed in Table 1 with two significant digits.

Notably, in both Figures S1 and S2, the samples were measured up to pH=11 (not shown) to highlight actual pK<sub>a</sub> values. All samples are stable and deprotonated in pH=10 aqueous solution.

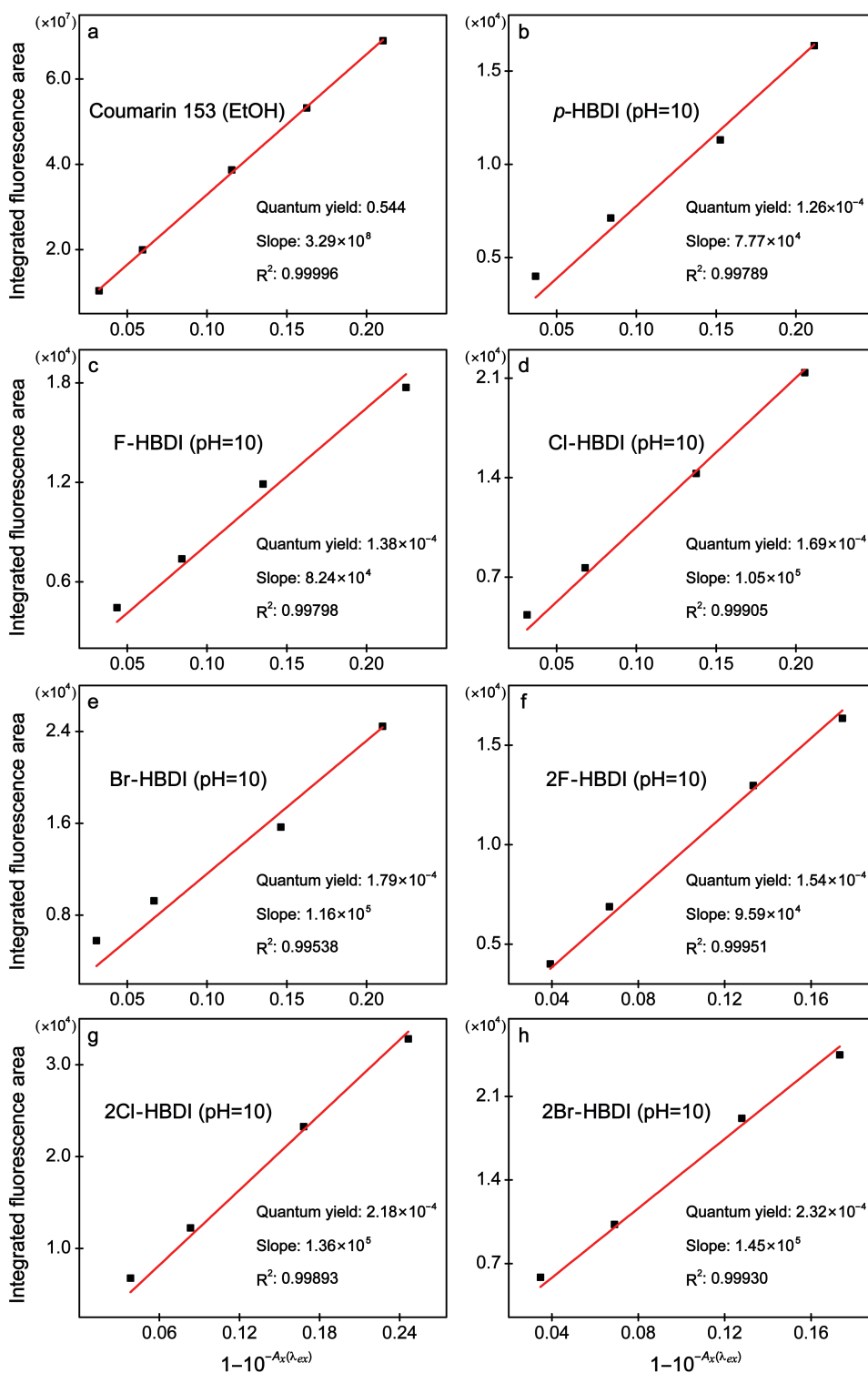


**Figure S3.** Determination of the fluorescence quantum yield (FQY) of HBDI derivatives. The integrated area for fluorescence signal intensity (from 485–635 nm upon 400 nm excitation) plotted against the absorption term at the excitation wavelength  $\lambda_{ex}$  for (a) Coumarin 153 in EtOH,

and (b) *p*-HBDI, (c-e) mono-, and (d-h) dihalogenated HBDI derivatives in pH=10 aqueous solution. Black squares represent data points at various sample concentrations, and red straight lines represent the least-squares linear fits. The corresponding FQY values, slopes, and  $R^2$  values (all close to unity) are listed within each panel.<sup>6,7</sup>

The zero *y*-intercept data point was included in data analysis while it is not shown in the plots above. Three independent measurements yielded a  $\pm 4\%$  range of the FQY values, whether or not the zero *y*-intercept data point was included. Due to low emission photon counts, the water scattering band was manually removed by Gaussian fitting. This could result in the  $\pm 4\%$  range of the FQY values as mentioned above; however, in all cases the FQY trend observed is consistent (Table 1) and thus used to help interpret the ultrafast spectroscopic results discussed in main text.

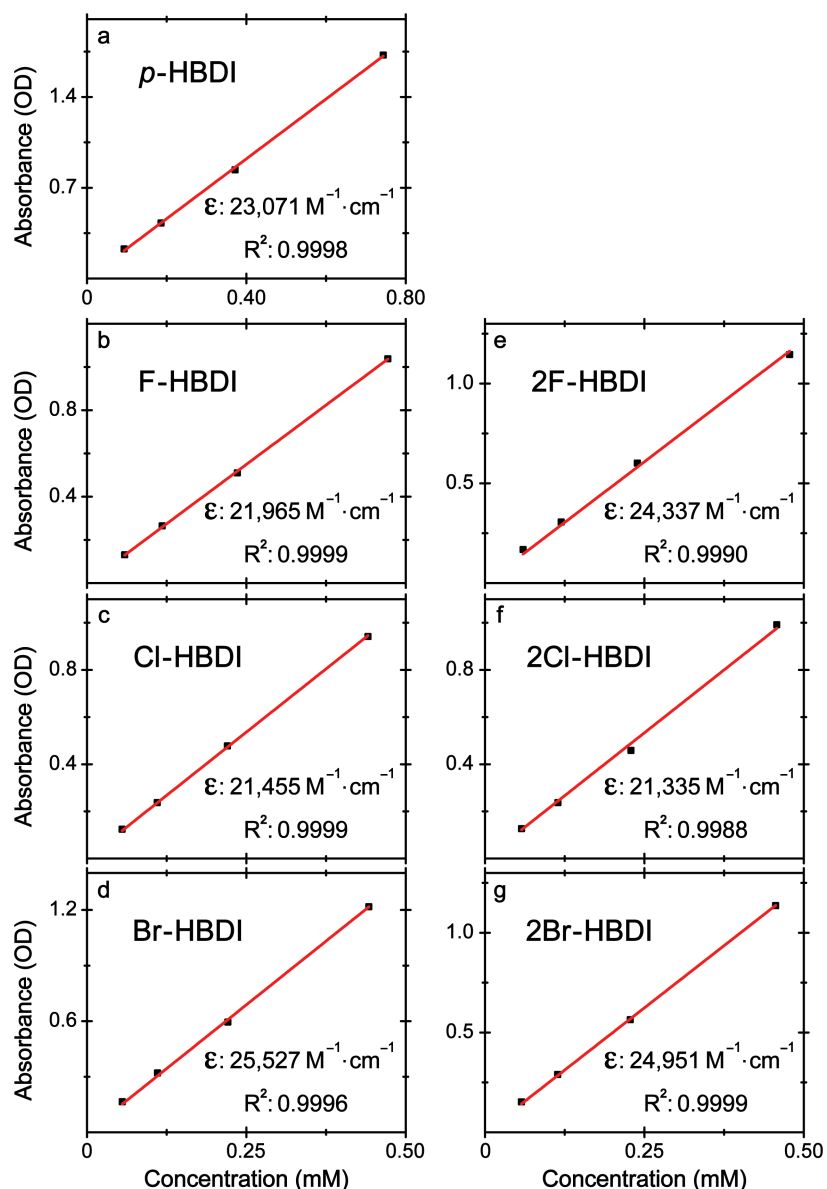


**Figure S4.** Determination of molar extinction coefficients of HBDI derivatives. The electronic absorbance plotted against the concentration for (a) *p*-HBDI, (b-d) mono-, and (e-g) dihalogenated HBDI derivatives in pH=10 aqueous solution using a 1-mm-pathlength quartz cuvette. Black squares represent data points at various concentrations, and red straight lines represent the least-squares linear fits. The corresponding molar extinction coefficient ( $\epsilon$ , calculated from the absorption value at 400 nm) and  $R^2$  values are listed within each panel. Due to the experimental errors associated with such measurements, the rounded values are tabulated in Table 1 (main text).

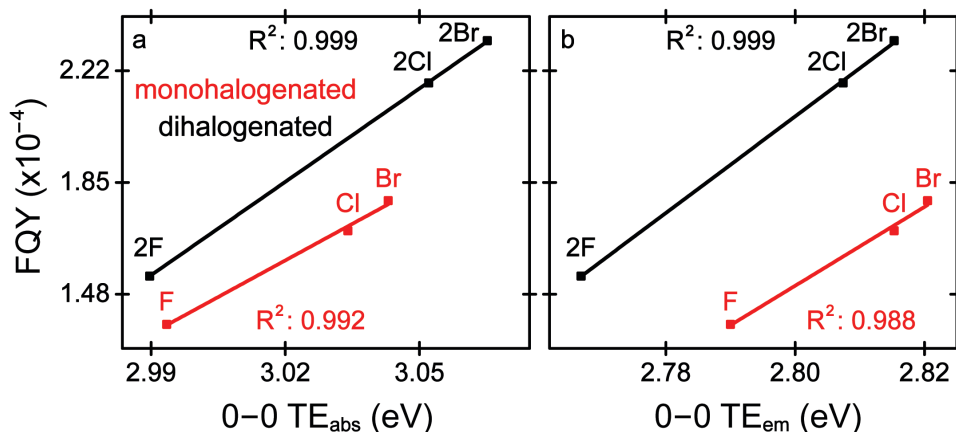


**Figure S5.** Fluorescence properties have an electronic origin. Correlation of FQY vs. the 0–0 TE (represented by HOMO–LUMO) transition energy gap for the calculated (a) absorption and (b) emission maximum values for the mono- (red) and dihalogenated (black) anionic HBDD derivatives. The TE values were determined from TD-DFT calculations (see Experimental methods section in main text). The  $R^2$  values are color-coded with respect to mono- and dihalogenated HBDD derivatives and displayed in each panel to show a strong correlation.

The calculated absorption and emission peak maxima (see Table 1 in main text) were taken from the output spectra with all the allowed electronic transitions from TD-DFT calculations with default peak broadening in Gaussian software;<sup>8</sup> therefore, those values differ from the 0–0 transition energies as represented by the HOMO–LUMO energy gaps (essentially responsible for the observed intense  $S_0 \rightarrow S_1$  absorption band that corresponds to a single  $\pi \rightarrow \pi^*$  transition)<sup>9–12</sup> displayed here. In contrast to a negative correlation between FQY and the experimental absorption peak energy (Figure 3a), a positive correlation between FQY and the calculated 0–0 TE suggests a complex excited-state potential energy surface that differs for its halogenation dependence in the Franck-Condon region (initially populated excited state) versus the fluorescence emission region (energy relaxed state). Nevertheless, the uncovered strong correlation between FQY and these experimental and theoretical energy gaps substantiate the underlying electronic origin.<sup>13,14</sup>

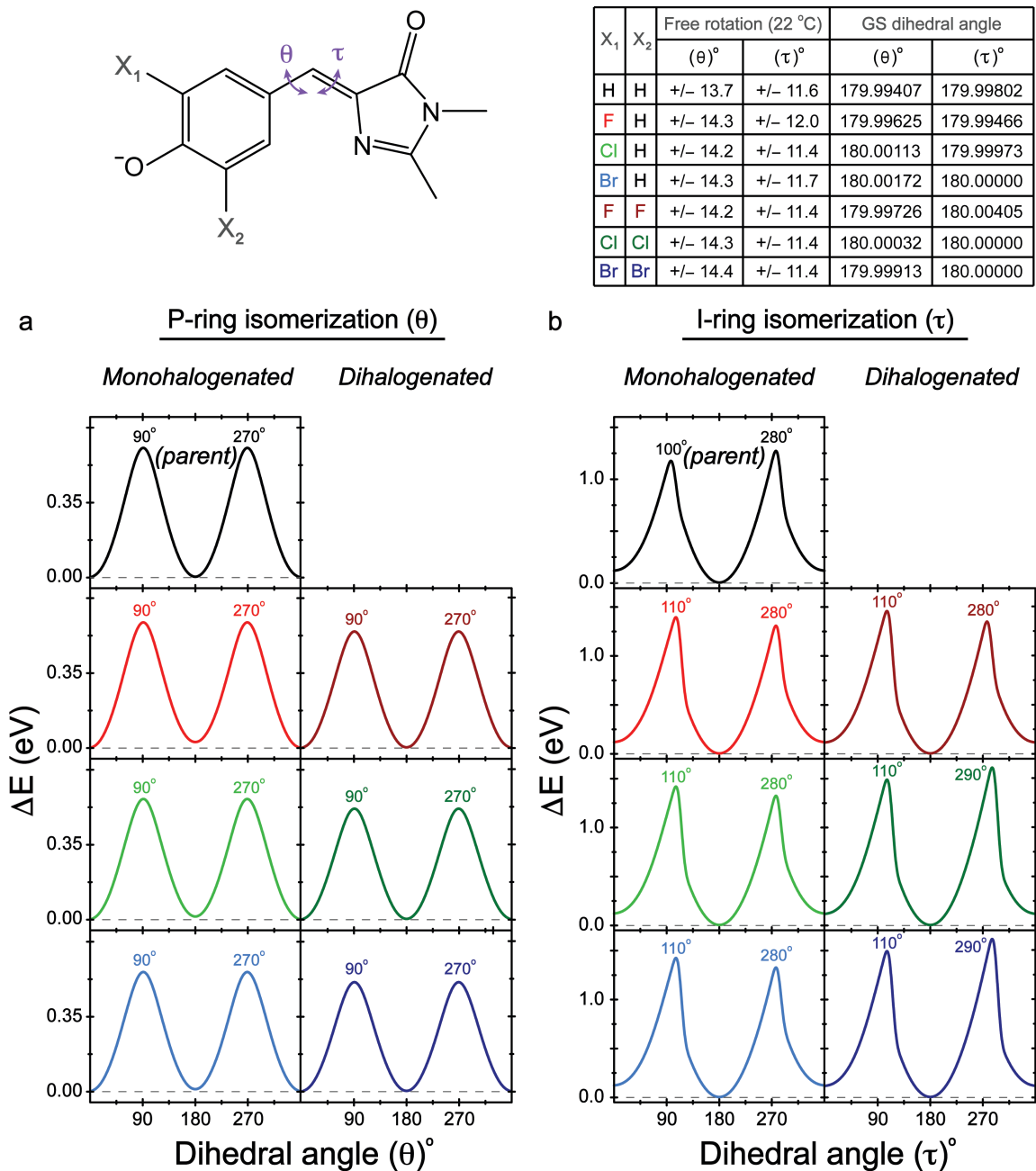


**Figure S6.** Ground-state electronic energy change as a function of methine bridge twisting angles. Energy change from the *cis* form plotted against the dihedral angle of the anionic *p*-HBDI and mono- and dihalogenated HBDI derivatives twisting along the (a) phenolate and (b) imidazolinone ring coordinates (see chemical structure and twisting angles in the upper left corner) in the ground state ( $S_0$ ) from DFT calculations. The table in the upper right corner shows free rotation at room

temperature ( $k_B T \approx 0.02543 \text{ eV}$ ,  $T = 295 \text{ K}$ ) along the P- and I-ring twisting coordinates and the optimized ground-state dihedral angles for the parent *p*-HBDI and each HBDI derivative. The spectral lines and abbreviations for each HBDI derivative are color-coded according to the substituents (hydrogen, H, black; fluorine, F, red; chlorine, Cl, green; bromine, Br, blue; 2F, dark red; 2Cl, dark green; and 2Br, dark blue). Dihedral angles that correspond to peak energy values are notated in each panel:  $\theta$ , CCCC dihedral that involves two carbon atoms on the P-ring;  $\tau$ , CCCC dihedral that involves two carbon atoms (terminating at the carbonyl site) on the I-ring.

Interestingly, upon I-ring twist in  $S_0$ , the energy minimum is achieved at  $\tau = 180^\circ$  (not  $0^\circ$  or  $360^\circ$  that shows a notably higher energy). For comparison, upon P-ring twist in  $S_0$ , the energy minimum is achieved at  $\theta = 0^\circ$  or  $360^\circ$  for the monohalogenated HBDI derivatives but that is within thermal energy (25.43 meV) of the  $180^\circ$  case (e.g., F-HBDI, 24.72 meV; Cl-HBDI, 10.53 meV; Br-HBDI, 8.25 meV). Moreover, only the bond connecting to the imidazolinone ring (bridge torsion coordinate -  $\tau$  angle) can act as a *cis-trans* isomeric switch between distinct populations of the anionic HBDI chromophores and derivatives; in contrast, torsion around the  $\theta$  angle maintains the phenolate  $-O^-$  group at the *para* site that does not affect the isomeric state.<sup>10,15</sup> In particular, the twisted intramolecular charge transfer (TICT) states via these bridge torsions are known to decrease the  $S_1/S_0$  energy gap and promote efficient energy dissipation pathways (see Figure 6 in main text).<sup>13,16,17</sup>

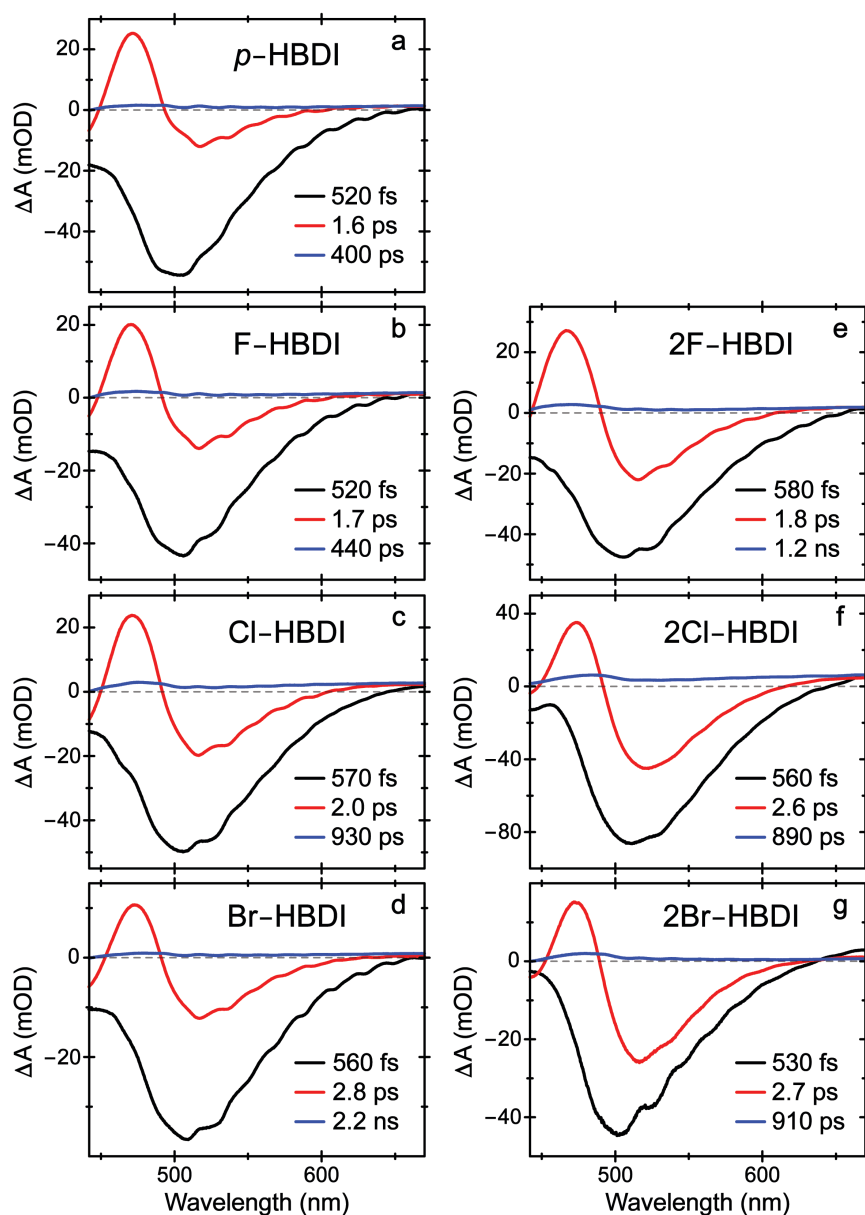


**Figure S7.** Global analysis of fs-TA spectra of the halogenated GFP chromophore derivatives. Deconvolved spectra with associated lifetimes are listed for the anionic (a) *p*-HBDI, (b-d) mono-, and (e-f) dihalogenated HBDI derivatives in pH=10 aqueous solution following 400 nm excitation. The evolution-associated difference spectra (EADS) with a sequential kinetic model yield three major components (color-coded) in the order of black→red→blue.<sup>18,19</sup> The negative and positive values (change of the absorbance in milli-OD unit) denote an SE and ESA (or hot ground-state absorption/HGSA)<sup>12</sup> band, respectively (not shown in main text due to similarity to *p*-HBDI).<sup>12</sup>

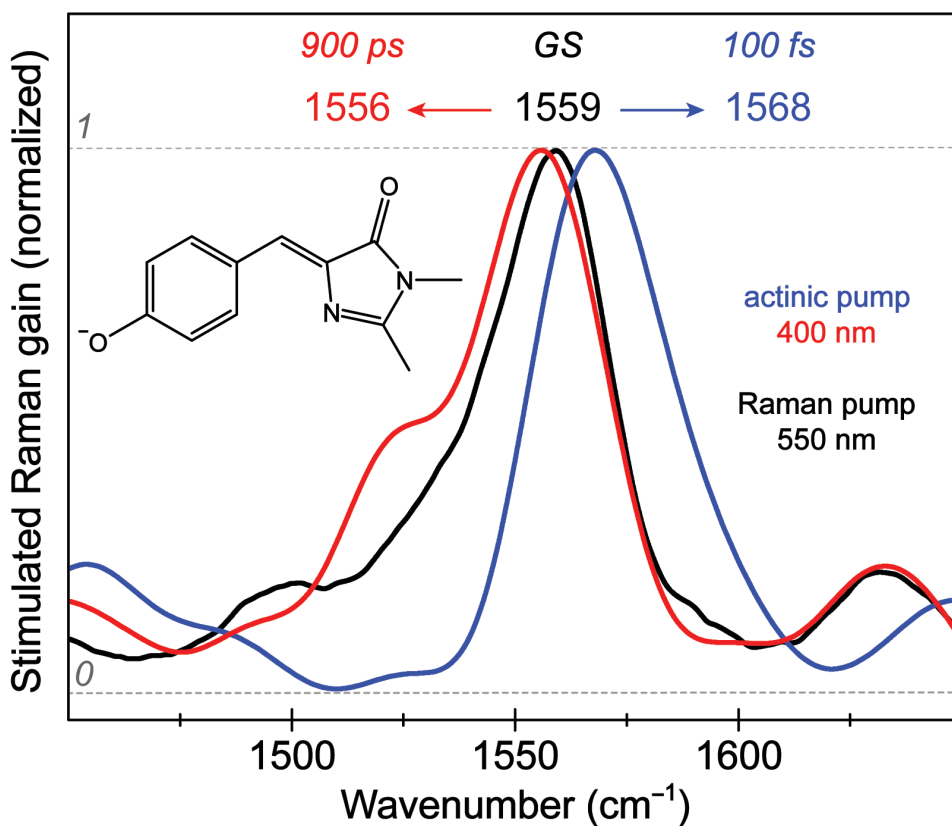


**Figure S8.** Normalized GS- and ES-FSRS spectra of anionic *p*-HBDI in pH=10 aqueous solution. The chromophore chemical structure is shown in the left inset. Data traces are color-coded according to the GS (black) and ES (100 fs, blue; 900 ps, red). For ES-FSRS, the actinic pump was tuned to 400 nm; for both GS- and ES-FSRS, the Raman pump was tuned to 550 nm. The Raman peak highlighted near 1560 cm<sup>-1</sup> shows the vibrational frequency change from GS to early (blueshift) and late (redshift) ES. The typically smaller ES-FSRS spectra<sup>12,13</sup> (blue and red) were normalized to the GS-FSRS peak at 1559 cm<sup>-1</sup> for easy comparison. A fast Fourier transform (FFT) smoothing function with 10 points was used for the ES spectra to reduce noise.

## ESI Tables

**Table S1.** Steady-state electronic spectroscopy and simplified Strickler-Berg equation data of properties for the parent, mono-, and di-halogenated HBDI derivatives in pH=10 aqueous solution

Sample	$E_{FC}$ (eV) <sup>a</sup>	Stokes shift (eV)	0–0 TE <sub>abs</sub> (eV) <sup>b</sup>	0–0 TE <sub>em</sub> (eV) <sup>b</sup>	$\Phi_F$ ( $\times 10^{-4}$ )	$k_F$ (ns <sup>-1</sup> ) <sup>c</sup>	$k_{nr}$ (ps <sup>-1</sup> ) <sup>d</sup>	$\tau_{nr}$ (fs) <sup>e</sup>	$f_{em, calc}$ <sup>f</sup>
<b><i>p</i>- HBDI</b>	2.917	0.418	3.013	2.817	1.26	0.293	2.325	430	1.2601
<b>F- HBDI</b>	2.938	0.448	2.999	2.790	1.38	0.280	2.026	494	1.2286
<b>Cl- HBDI</b>	2.924	0.424	3.037	2.815	1.69	0.292	1.729	578	1.2609
<b>Br- HBDI</b>	2.917	0.423	3.046	2.820	1.79	0.295	1.646	607	1.2762
<b>2F- HBDI</b>	2.966	0.466	2.996	2.767	1.54	0.279	1.811	552	1.2204
<b>2Cl- HBDI</b>	2.938	0.453	3.054	2.807	2.18	0.276	1.269	788	1.2206
<b>2Br- HBDI</b>	2.931	0.451	3.066	2.815	2.32	0.277	1.195	837	1.2283

<sup>a</sup> Measured from the experimental absorption peak maximum (Figure 1, Table 1 in main text).<sup>14</sup>

<sup>b</sup> The 0–0 transition energy (TE) for absorption (abs.) and emission (em.) is represented by the HUMO–LUMO energy gap from the corresponding TD-DFT calculations.<sup>20–22</sup>

<sup>c</sup> Determined from the simplified Strickler-Berg equation<sup>23</sup> (Equation 1 in main text) on the basis of radiative transition probabilities. Since these HBDI derivatives exhibit very dim fluorescence, time constants retrieved from femtosecond transient absorption (fs-TA) spectra are convoluted with dominant nonradiative pathways. This column of rate constants ( $k_F=k_r$ ) corresponds to fluorescence lifetimes of ca. 3.4–3.6 ns, typical for this series of organic chromophores.<sup>13,24,25</sup>

<sup>d</sup> Determined from the definition of FQY and the derived expression (Equation 3 in main text).

<sup>e</sup> Obtained from the inverse of  $k_{nr}$  with the proper unit conversion (1 ps = 1000 fs). Notably, for dim chromophores ( $\Phi_F \ll 1$ ),  $k_{nr}$  determines the apparent lifetime of fluorescent state (Figure S7).

<sup>f</sup> Oscillator strength ( $f$ ) taken from the emitting state from TD-DFT calculations.

**Table S2.** Experimental ground-state Raman mode frequencies and assignments aided by quantum calculations for *p*-HBDI and the monohalogenated HBDI derivatives

Raman mode assignment <sup>a</sup>	<i>p</i> -HBDI		F-HBDI		Cl-HBDI		Br-HBDI	
	exp. <sup>b</sup>	cal. <sup>c</sup>						
I-ring and weak P-ring i.p. deformation	611	595	617	607	616	603	613	602
I-ring i.p. deformation, P-ring breathing with C–X <sup>d</sup> stretch, and weak bridge CCC bending	848	828	923	904	905	867	886	854
	924	920		944		927		925
I-ring i.p. deformation with CCH and NCH bending, weak P-ring C–H rocking	1034	1022	1036	1022	1035	1024	1033	1024
P-ring i.p. C–H scissoring, bridge C–H rocking, I-ring i.p. deformation	1170	1178	1143	1142	1140	1138	1137	1137
P-ring i.p. deformation, bridge C–C stretch	-	-	1217	1202	1217	1207	1216	1206
P-ring i.p. deformation and C–H scissoring, bridge C–H rocking	1243	1246	1259	1252	1252	1241	1253	1241
P-ring and bridge C–H rocking, I-ring deformation	1305	1293	1309	1291	1312	1289	1308	1289
P-ring and bridge C–H rocking, I-ring C–N stretch and i.p. deformation	1373	1372	-	-	-	-	-	-
P-ring asymmetric C=C and bridge CCC stretch	1442	1459 <sup>e</sup>	1451	1452	1420	1479	1418	1472
P-ring C=O stretch and bridge CCC stretch	1499	1500 <sup>e</sup>	1498	1506	1488	1507	1485	1506
P-ring C=C and C=O stretch, bridge CCC stretch, weak I-ring C=N and C=O stretch	1559	1545	1566	1557	1561	1550	1560	1548
P-ring symmetric C=C stretch, bridge CCC stretch, I-ring C=O and C=N stretch	1633	1622	1640	1629	1636	1621	1633	1619

<sup>a</sup> Raman mode assignments of major atomic motions of the chromophores (listed in order of most intense to least intense) are aided by quantum calculations. P- and I-ring denotes the phenolate and imidazolinone ring, respectively, and i.p. denotes in-plane (see the chemical structures in Fig. 1a).

<sup>b</sup> The GS Raman peak frequencies (in  $\text{cm}^{-1}$  unit) of the anionic *p*-HBDI and its monohalogenated derivatives in pH=10 aqueous solution as determined from GS-FSRS experiments using 550 nm Raman pump and a white-light probe (see Fig. 4a-d in main text).<sup>12</sup>

<sup>c</sup> Vibrational normal mode frequencies of the anionic chromophores were calculated from the geometrically optimized structure in the electronic ground state  $S_0$  using Gaussian software (see Experimental methods section in main text) with a frequency scaling factor of 0.985.<sup>12,26,27</sup>

<sup>d</sup> C-X stands for the single carbon-halogen bond ( $X = \text{F}, \text{Cl}, \text{Br}$ ) in monohalogenated HBDI derivatives. Some adjacent vibrational modes appear for *p*-HBDI in solution and sfGFP as well.<sup>28</sup>

<sup>e</sup> These two largely localized P-ring C=C and C=O stretching in conjunction with bridge C=C stretching modes at  $\sim 1459$  and  $1500 \text{ cm}^{-1}$  exhibit a frequency redshift to  $\sim 1438$  and  $1453 \text{ cm}^{-1}$  (from TD-DFT calculations, see Table S4 below for more details), respectively, which is in accord with the prompt ICT from P to I ring of the anionic HBDI chromophore (Fig. 6 inset, main text). Due to their weak Raman peak intensities in the experimental FSRS data that hinder a strong assignment of the photoinduced vibrational frequency change (Fig. 4), we instead focus on main peak frequency blueshift of the  $\sim 1560 \text{ cm}^{-1}$  mode as observed (Fig. 4) as well as calculated (Tables S2 and S4) for the more delocalized double-bond stretching motions across the two-ring system.

**Table S3.** Experimental ground-state Raman mode frequencies and assignments aided by quantum calculations for the dihalogenated HBDI derivatives

Raman mode assignment <sup>a</sup>	2F-HBDI		2Cl-HBDI		2Br-HBDI	
	exp. <sup>b</sup>	cal. <sup>c</sup>	exp. <sup>b</sup>	cal. <sup>c</sup>	exp. <sup>b</sup>	cal. <sup>c</sup>
I-ring and weak P-ring i.p. deformation	593	583	599	583	581	570
I-ring i.p. deformation, P-ring breathing with symmetric C-X <sup>d</sup> stretch, weak bridge CCC bending	922	914	914	899	902	880
		959		934		927
I-ring i.p. deformation with CCH and NCH bending, weak P-ring C-H rocking	1038	1027	1037	1024	1035	1020
Bridge and P-ring C-H rocking, I-ring i.p. deformation	1131	1125	1141	1123	1138	1120
P-ring i.p. deformation with C-H rock, bridge C-C stretch with C-H rock	1268	1245	1228	1224	1224	1223
P-ring i.p. deformation and C-H rocking, bridge CCC bend, I-ring i.p. deformation	1305	1293	1305	1290	1304	1290
P-ring and bridge C-H rocking, I-ring C-N stretch	1348	1357	1340	1352	1333	1350
P-ring breathing with weak I-ring C-N stretch	1379	1393	1380	1395	-	1394
P-ring asymmetric C=C and bridge CCC stretch	1458	1448	1421	1434	1415	1429
P-ring C=O stretch, bridge i.p. CCC stretch	1504	1499	1477	1501	1462	1501
P-ring C=C and C=O stretch, bridge CCC stretch, I-ring C=N and weak C=O stretch	1566	1564	1562	1556	1559	1552
P-ring symmetric C=C stretch, bridge CCC stretch, and I-ring C=O and weak C=N stretch	1648	1632	1641	1621	1638	1619

<sup>a</sup> Raman mode assignment of major atomic motions of the chromophores (listed in order of most intense to least intense) are aided by quantum calculations. P- and I-ring denotes the phenolate and imidazolinone ring, respectively, and i.p. denotes in-plane (see the chemical structures in Fig. 1b).

<sup>b</sup> The GS Raman peak frequencies (in cm<sup>-1</sup> unit) for the anionic dihalogenated derivatives in pH=10 aqueous solution as determined from GS-FSRS experiments (see Fig. 4e-g in main text).

<sup>c</sup> Vibrational normal mode frequencies of the anionic chromophores were calculated from the geometrically optimized structure in the electronic ground state  $S_0$  using Gaussian software with a frequency scaling factor of 0.985 (see above).

<sup>d</sup> C–X stands for both carbon-halogen bonds ( $X = \text{F}, \text{Cl}, \text{Br}$ ) in dihalogenated HBDI derivatives.

**Table S4.** Selected experimental excited-state Raman mode frequencies and assignments aided by quantum calculations for *p*-HBDI and the monohalogenated HBDI derivatives

Raman mode assignment <sup>a</sup>	<i>p</i> -HBDI <sup>b</sup>		F-HBDI		Cl-HBDI		Br-HBDI	
	exp. <sup>c</sup>	cal. <sup>d</sup>	exp. <sup>c</sup>	cal. <sup>d</sup>	exp. <sup>c</sup>	cal. <sup>d</sup>	exp. <sup>c</sup>	cal. <sup>d</sup>
I-ring i.p. deformation, P-ring breathing with C–X <sup>e</sup> stretch, weak bridge CCC bending	-	-	935	917	956	873	895	858
				950		939		938
I-ring C=O and weak C=N stretch, P-ring symmetric C=C and C=O stretch <sup>f</sup>	1568	1561	1573	1565	1571	1562	1575	1562

<sup>a</sup> Major atomic motions of the chromophores (listed in order of most intense to least intense) as aided by quantum calculations in S<sub>1</sub>. P- and I-ring, phenolate and imidazolinone ring; i.p., in-plane.

<sup>b</sup> The excited-state Raman mode frequencies and assignments largely match our previous report on anionic *p*-HBDI in aqueous solution.<sup>12</sup> The focus of this paper is the halogenated derivatives.

<sup>c</sup> The excited-state peak frequency (in cm<sup>-1</sup> unit) is subject to baseline drawing and may be affected by the 10-point FFT smoothing function used to reduce the spectral noise at ~100 fs time delay (Figure S8).<sup>12,13</sup> The corresponding ground-state Raman peak frequencies for the anionic *p*-HBDI and its monohalogenated derivatives are listed in Table S2 (also see Figure 4a-d in main text).

<sup>d</sup> Vibrational normal mode frequencies as calculated from the geometrically optimized anionic chromophores using the TD-DFT method (see Experimental method section in main text) with frequency scaling factors of 0.97 and 1.01 for high- and low-frequency modes, respectively.<sup>12,22,27,29</sup> Two adjacent modes with similar composition including the C–X stretch from calculations are listed.<sup>28</sup>

<sup>e</sup> C–X stands for the single carbon-halogen bond (X = F, Cl, Br).

<sup>f</sup> The slight change in mode composition from S<sub>0</sub> (e.g., 1559/1545 cm<sup>-1</sup> for exp./cal. frequencies of *p*-HBDI in Table S2) arises from the prompt electron redistribution within Franck-Condon region as corroborated by the electron density map change from HOMO to LUMO (Fig. 2 in main text).

**Table S5.** Selected experimental excited-state Raman mode frequencies and assignments aided by quantum calculations for the dihalogenated HBDI derivatives

Raman mode assignment <sup>a</sup>	2F-HBDI		2Cl-HBDI		2Br-HBDI	
	exp. <sup>b</sup>	cal. <sup>c</sup>	exp. <sup>b</sup>	cal. <sup>c</sup>	exp. <sup>b</sup>	cal. <sup>c</sup>
I-ring i.p. deformation with C–N stretch, P-ring breathing with symmetric C–X <sup>d</sup> stretch, weak bridge CCC bending	927	934	927	908	908	885
		969		941		938
I-ring C=O and weak C=N stretch, P-ring symmetric C=C and C=O stretch	1573	1569	1571	1566	1568	1566

<sup>a</sup> Major atomic motions of the chromophores (listed in order of most intense to least intense) as aided by quantum calculations in S<sub>1</sub>. P- and I-ring, phenolate and imidazolinone ring; i.p., in-plane.

<sup>b</sup> The excited-state peak frequency (in cm<sup>-1</sup> unit) is subject to baseline drawing and may be affected by the 10-point FFT smoothing function used to reduce the spectral noise at ~100 fs time delay. The corresponding ground-state Raman peak frequencies for the dihalogenated HBDI derivatives are listed in Table S3 (also see Figure 4e-g in main text).

<sup>c</sup> Vibrational normal mode frequencies as calculated from the geometrically optimized anionic chromophores using the TD-DFT method (see Experimental method section in main text) with frequency scaling factors of 0.97 and 1.01 for high- and low-frequency modes, respectively. Two adjacent modes with similar composition including C–X stretch from calculations are listed.<sup>28</sup>

<sup>d</sup> C–X stands for both carbon-halogen bonds (X = F, Cl, Br).

**Table S6.** Calculated natural bond orbital (NBO) charges for the P-ring, methine bridge, and I-ring to examine the percent change of ICT from the GS/FC to FS state

Sample	GS/FC <sup>a</sup>			FS <sup>b</sup>			GS/FC → FS		
	P-ring	methine bridge	I-ring	P-ring	methine bridge	I-ring	P-ring	methine bridge	I-ring
<i>p</i> -HBDI	-0.743	0.168	-0.425	-0.720	0.166	-0.446	3.10% (0.023)	-1.19% (-0.002)	-4.94% (-0.021)
F-HBDI	-0.776	0.169	-0.393	-0.746	0.167	-0.421	3.87% (0.030)	-1.18% (-0.002)	-7.12% (-0.028)
Cl-HBDI	-0.788	0.172	-0.383	-0.757	0.171	-0.414	3.93% (0.031)	-0.58% (-0.001)	-8.09% (-0.031)
Br-HBDI	-0.788	0.172	-0.382	-0.756	0.171	-0.413	4.06% (0.032)	-0.58% (-0.001)	-8.12% (-0.031)
2F-HBDI	-0.805	0.170	-0.365	-0.771	0.163	-0.392	4.22% (0.034)	-4.12% (-0.007)	-7.40% (-0.027)
2Cl-HBDI	-0.823	0.174	-0.351	-0.788	0.173	-0.385	4.25% (0.035)	-0.57% (-0.001)	-9.69% (-0.034)
2Br-HBDI	-0.828	0.175	-0.348	-0.794	0.175	-0.382	4.11% (0.034)	-	-9.77% (-0.034)

<sup>a</sup>The NBO charges for the optimized GS structures of anionic chromophores were calculated with DFT; NBO charges for Franck-Condon (FC) region were from the energy calculation with TD-DFT method using the optimized GS structure. Both calculations used the RB3LYP functional and 6-311G+(d,p) basis set. More negative charges on P ring are seen from mono- to dihalogenation.

<sup>b</sup>The NBO charges for the fluorescent state (FS) state were determine from the TD-DFT method with RB3LYP functional and 6-311G+(d,p) basis set of the geometrically optimized structure in the first singlet excited state (S<sub>1</sub>). Green and red colors represent the decreasing and increasing negative charges on those moieties, respectively.

Notably, the total NBO charges for each moiety (P-ring, methine bridge that only consists of the center C and H atoms, and I-ring) of the chromophore were determined by summation of the individual charges on each atom; the grand total charge is -1 for the anionic chromophore. The GS/FC NBO charges were identical due to the Born-Oppenheimer approximation: there is no

geometrical rearrangement during vertical excitation of the optimized GS structure and our current level of theory is inadequate to account for “instantaneous” electron redistribution in this region.<sup>9</sup> The numbers in green (red) represent an increase (decrease) in the absolute value from the GS/FC, i.e., a decrease (increase) in electron density. Therefore, the total changes in parentheses add to zero (last three columns) due to the P-to-I-ring ICT and the conserved total electric charge of  $-1$ .

In all the HBDI derivatives being calculated, there is loss of electron density on the P-ring and gain of electron density on the methine bridge (small change, ca. 1–4%) and I-ring (more notable change, ca. 5–10%). This is in accord with an ICT process from the FC to FS, with the extent of ICT increasing from the parent HBDI to mono- to di-halogenated HBDI in the order of  $F < Cl < Br$ . Interestingly, a previous report proposed that H-bonds between protic solvents (e.g., water as H-bond donor) and the HBDI imidazolinone group (e.g., N or O site as H-bond acceptor) could quench fluorescence to some extent,<sup>30</sup> and the photoinduced ICT from the P ring to I ring enhances such an effect. This interpretation does not work in the halogenated HBDI derivatives because as ICT increases with larger halogens, the FQY increases not only in aqueous solution (this work, see Tables 1 and S1) but also inside a protein pocket (e.g., superfolder-GFP).<sup>28</sup> This result could be specific to the anionic chromophore in polar and protic solvents like water (our focus here) that exhibits a dominant I-ring-twist-induced access to an  $S_1/S_0$  CI (Fig. 6 in main text) and the resultant *cis-to-trans* isomerization as one of the relaxation pathways, while the negative charge is still largely present on the P ring in  $S_1$  (see Table S6, despite the photoinduced ICT).<sup>10,12,15,24,31</sup>

NBO charge analysis was chosen over Mulliken charge analysis since NBO is less sensitive to the basis set choice and is considered more realistic due to a localized Lewis-like molecular bonding and reactivity pattern for one-center lone pairs and two-center bonds. Therefore, NBO charge analysis provides a valence bond-type description of the electronic wavefunction.<sup>22,32,33</sup>

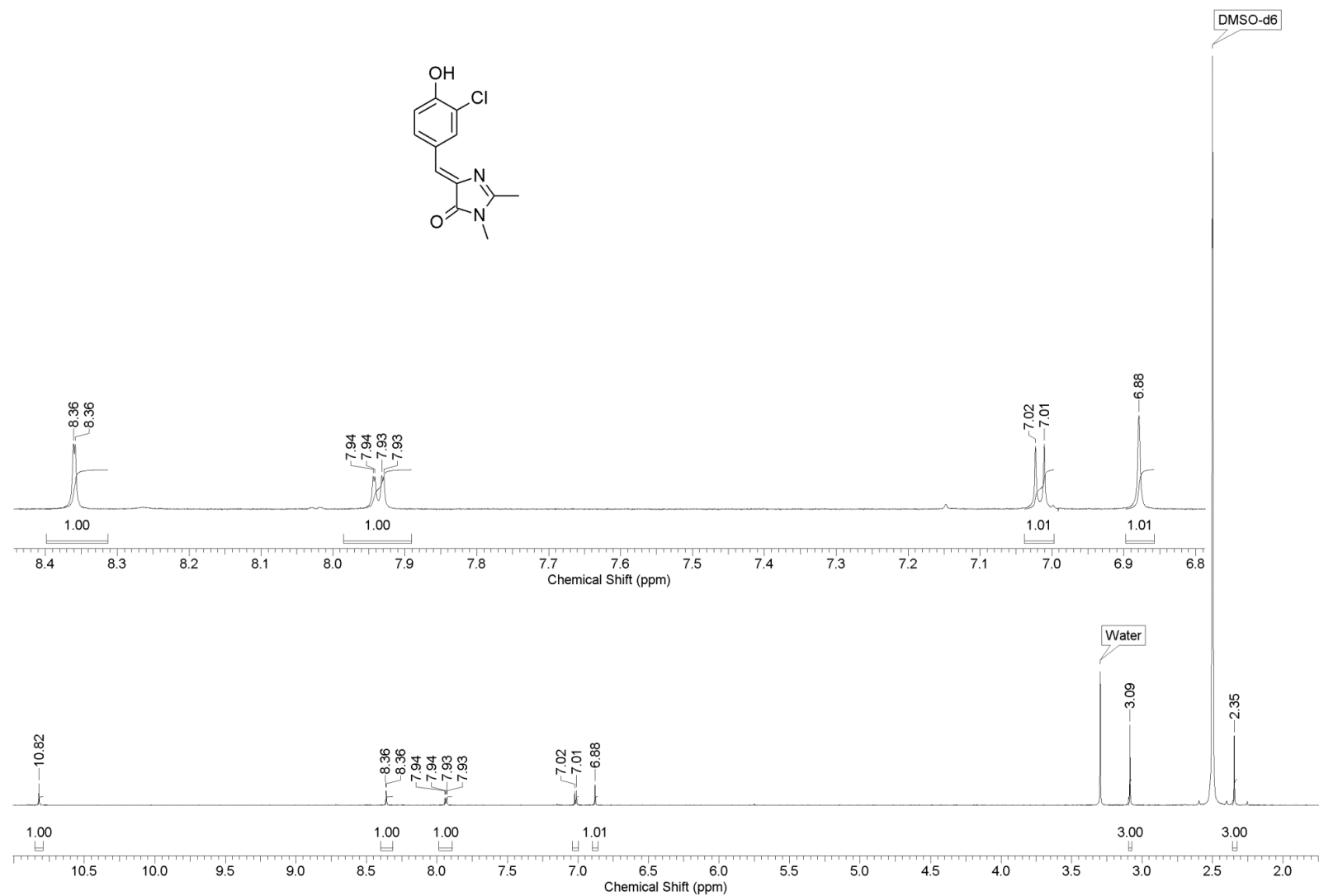
## ESI References

- 1 A. I. Meyers, J. P. Lawson, D. G. Walker and R. J. Linderman, *J. Org. Chem.*, 1986, **51**, 5111-5123.
- 2 C. Chen, L. Zhu, S. A. Boulanger, N. S. Baleeva, I. N. Myasnyanko, M. S. Baranov and C. Fang, *J. Chem. Phys.*, 2020, **152**, 021101.
- 3 C. Chen, W. Liu, M. S. Baranov, N. S. Baleeva, I. V. Yampolsky, L. Zhu, Y. Wang, A. Shamir, K. M. Solntsev and C. Fang, *J. Phys. Chem. Lett.*, 2017, **8**, 5921–5928.
- 4 W. Song, R. L. Strack, N. Svensen and S. R. Jaffrey, *J. Am. Chem. Soc.*, 2014, **136**, 1198-1201.
- 5 K. Lincke, T. Sølling, L. H. Andersen, B. Klærke, D. B. Rahbek, J. Rajput, C. B. Oehlenschläger, M. Å. Petersen and M. B. Nielsen, *Chem. Commun.*, 2010, **46**, 734-736.
- 6 K. Rurack and M. Spieles, *Anal. Chem.*, 2011, **83**, 1232-1242.
- 7 T. D. Krueger, S. A. Boulanger, L. Zhu, L. Tang and C. Fang, *Struct. Dyn.*, 2020, **7**, 024901.
- 8 M. J. Frisch, G. W. Trucks, H. B. Schlegel, G. E. Scuseria, M. A. Robb, J. R. Cheeseman, G. Scalmani, V. Barone, B. Mennucci, G. A. Petersson, H. Nakatsuji, M. Caricato, X. Li, H. P. Hratchian, A. F. Izmaylov, J. Bloino, G. Zheng, J. L. Sonnenberg, M. Hada, M. Ehara, K. Toyota, R. Fukuda, J. Hasegawa, M. Ishida, T. Nakajima, Y. Honda, O. Kitao, H. Nakai, T. Vreven, J. J. A. Montgomery, J. E. Peralta, F. Ogliaro, M. Bearpark, J. J. Heyd, E. Brothers, K. N. Kudin, V. N. Staroverov, R. Kobayashi, J. Normand, K. Raghavachari, A. Rendell, J. C. Burant, S. S. Iyengar, J. Tomasi, M. Cossi, N. Rega, J. M. Millam, M. Klene, J. E. Knox, J. B. Cross, V. Bakken, C. Adamo, J. Jaramillo, R. Gomperts, R. E. Stratmann, O. Yazyev, A. J. Austin, R. Cammi, C. Pomelli, J. W. Ochterski, R. L. Martin, K. Morokuma, V. G. Zakrzewski, G. A. Voth, P. Salvador, J. J. Dannenberg, S. Dapprich, A. D. Daniels, Ö. Farkas,

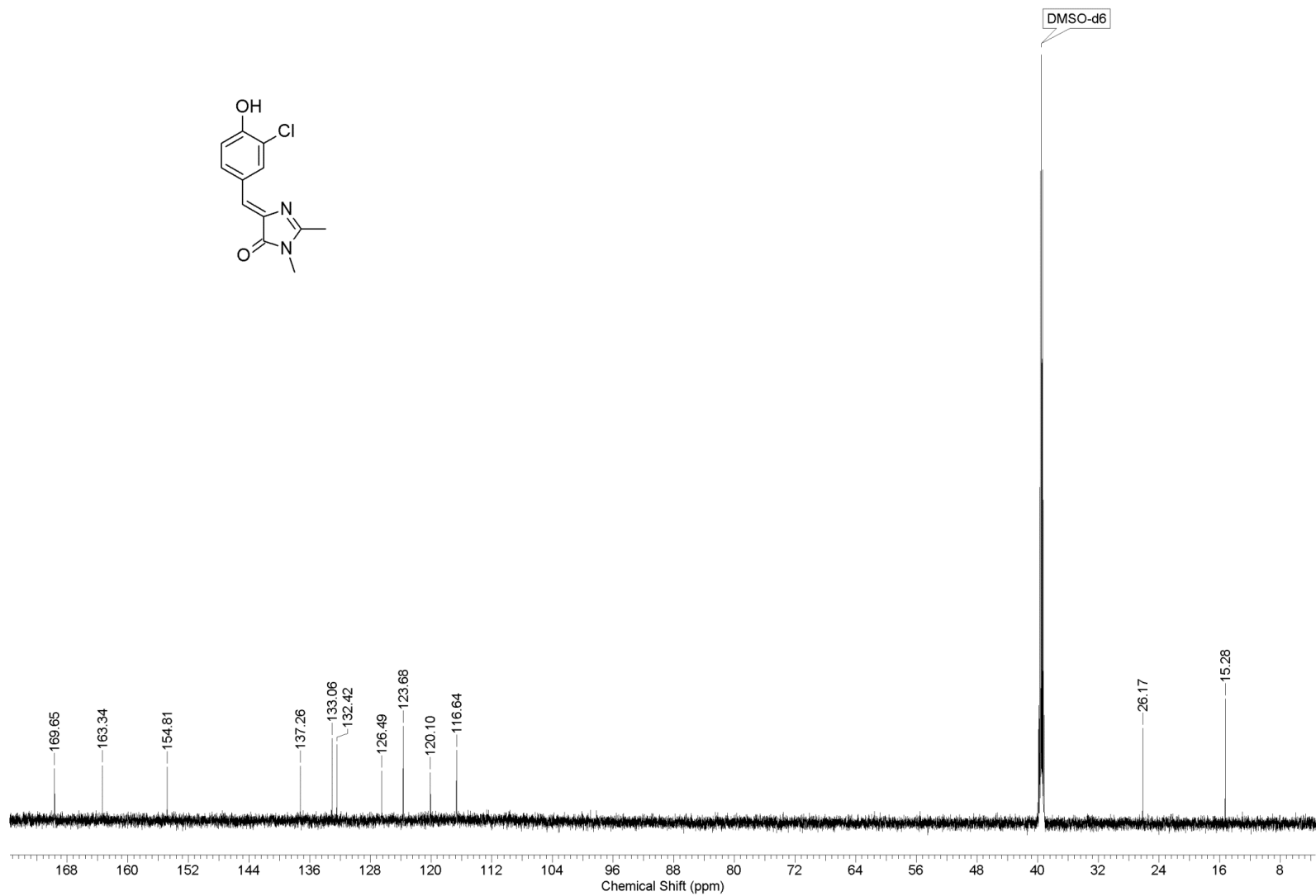
- J. B. Foresman, J. V. Ortiz, J. Cioslowski and D. J. Fox, *Gaussian 09, Revision B.1*, Gaussian, Inc., Wallingford, CT, 2009.
- 9 M. E. Martin, F. Negri and M. Olivucci, *J. Am. Chem. Soc.*, 2004, **126**, 5452-5464.
  - 10 P. Altoe, F. Bernardi, M. Garavelli, G. Orlandi and F. Negri, *J. Am. Chem. Soc.*, 2005, **127**, 3952-3963.
  - 11 G. Haberhauer, R. Gleiter and C. Burkhardt, *Chem. Eur. J.*, 2016, **22**, 971-978.
  - 12 M. A. Taylor, L. Zhu, N. D. Rozanov, K. T. Stout, C. Chen and C. Fang, *Phys. Chem. Chem. Phys.*, 2019, **21**, 9728-9739.
  - 13 C. Fang, L. Tang and C. Chen, *J. Chem. Phys.*, 2019, **151**, 200901.
  - 14 M. G. Romei, C.-Y. Lin, I. I. Mathews and S. G. Boxer, *Science*, 2020, **367**, 76-79.
  - 15 S. Olsen and S. C. Smith, *J. Am. Chem. Soc.*, 2008, **130**, 8677-8689.
  - 16 S. Sasaki, G. P. C. Drummen and G.-i. Konishi, *J. Mater. Chem. C*, 2016, **4**, 2731-2743.
  - 17 T. Kumpulainen, B. Lang, A. Rosspeintner and E. Vauthey, *Chem. Rev.*, 2017, **117**, 10826-10939.
  - 18 R. Berera, R. van Grondelle and J. M. Kennis, *Photosynth. Res.*, 2009, **101**, 105-118.
  - 19 J. J. Snellenburg, S. P. Liptonok, R. Seger, K. M. Mullen and I. H. M. van Stokkum, *J. Stat. Softw.*, 2012, **49**, 1-22.
  - 20 L. Tang, L. Zhu, M. A. Taylor, Y. Wang, S. J. Remington and C. Fang, *Molecules*, 2018, **23**, 2226.
  - 21 C. Chen, M. S. Baranov, L. Zhu, N. S. Baleeva, A. Y. Smirnov, S. Zaitseva, I. V. Yampolsky, K. M. Solntsev and C. Fang, *Chem. Commun.*, 2019, **55**, 2537-2540.
  - 22 C. Chen, L. Zhu, M. S. Baranov, L. Tang, N. S. Baleeva, A. Y. Smirnov, I. V. Yampolsky, K. M. Solntsev and C. Fang, *J. Phys. Chem. B*, 2019, **123**, 3804-3821.

- 23 S. J. Strickler and R. A. Berg, *J. Chem. Phys.*, 1962, **37**, 814-822.
- 24 D. Mandal, T. Tahara and S. R. Meech, *J. Phys. Chem. B*, 2004, **108**, 1102-1108.
- 25 R. Gepshtein, D. Huppert and N. Agmon, *J. Phys. Chem. B*, 2006, **110**, 4434-4442.
- 26 A. P. Esposito, P. Schellenberg, W. W. Parson and P. J. Reid, *J. Mol. Struct.*, 2001, **569**, 25-41.
- 27 J. P. Merrick, D. Moran and L. Radom, *J. Phys. Chem. A*, 2007, **111**, 11683-11700.
- 28 B. G. Oscar, L. Zhu, H. Wolfendeen, N. D. Rozanov, A. Chang, K. T. Stout, J. W. Sandwisch, J. J. Porter, R. A. Mehl and C. Fang, *Front. Mol. Biosci.*, 2020, **7**, 131.
- 29 A. P. Scott and L. Radom, *J. Phys. Chem.*, 1996, **100**, 16502-16513.
- 30 J.-S. Yang, G.-J. Huang, Y.-H. Liu and S.-M. Peng, *Chem. Commun.*, 2008, 1344-1346.
- 31 I. V. Polyakov, B. L. Grigorenko, E. M. Epifanovsky, A. I. Krylov and A. V. Nemukhin, *J. Chem. Theory Comput.*, 2010, **6**, 2377-2387.
- 32 F. Weinhold, *J. Comput. Chem.*, 2012, **33**, 2363-2379.
- 33 B. D. Dunnington and J. R. Schmidt, *J. Chem. Theory Comput.*, 2012, **8**, 1902-1911.

## ESI Appendix (NMR spectra of the new compound)



**Appendix S1.**  $^1\text{H}$  NMR spectrum of (Z)-5-(3-chloro-4-hydroxybenzylidene)-2,3-dimethyl-3,5-dihydro-4H-imidazol-4-one (**1c**)



**Appendix S2.** <sup>13</sup>C NMR spectrum of (Z)-5-(3-chloro-4-hydroxybenzylidene)-2,3-dimethyl-3,5-dihydro-4H-imidazol-4-one (**1c**)